Journal of Solid State Chemistry **166,** 42–48 (2002)
doi:10.1006/jssc.2002.9554, available online at http://www.idealibrary.com on IDEAL®

# Structure and Phase Transitions of $SnP_2O_7$

R. K. B Gover,* N. D. Withers,* S. Allen,* R. L. Withers,† and J. S. O. Evans*,[1]

*Department of Chemistry, University of Durham, South Road, Durham DH1 3LE, United Kingdom; and †Research School of Chemistry, Australian National University, Canberra ACT 0200, Australia

**$SnP_2O_7$ is a member of the $ZrP_2O_7$ family of materials, several of which show unusual thermal expansion behavior over certain temperature ranges and which show a number of displacive phase transitions on cooling from high temperature. Here we describe the structural properties of $SnP_2O_7$ from 100 to 1243 K as determined by X-ray and neutron powder diffraction. These studies reveal that $SnP_2O_7$ shows two phase transitions in this temperature range. At room temperature the material has a pseudo-cubic $3\times3\times3$ superstructure. Electron diffraction studies show that the symmetry of this structure is $P2_13$ or lower. On warming to $\sim 560$ K it undergoes a phase transition to a structure in which the subcell reflections show a triclinic distortion; above 830 K the subcell reflections show a rhombohedral distortion. Significant hysteresis in cell parameters is observed between heating and cooling. The structure of $SnP_2O_7$ is discussed with references to other members of the $AM_2O_7$ family of materials.** 

***Key Words:*** **tin pyrophosphate; thermal expansion; X-ray diffraction; electron diffraction; neutron diffraction; phase transitions.**

## INTRODUCTION

Since the discovery of unusual thermal expansion in $ZrV_{2-x}P_xO_7$ and related phases (1–3), there has been considerable interest in compounds of the general type $AM_2O_7$ ($A$ = Ti, Zr, Hf, Mo, W, Re, Si, Ge, Pb, Sb, Ce, Th, U, Np and Pu, $M$ = V, P and As) (4–7). Low thermal expansion materials have a range of uses in ceramic, electronic and optical applications. $AM_2O_7$ phases were initially thought to have the simple cubic structure shown in Fig. 1 (8), which can be described in terms of corner sharing $AO_6$ octahedra and $MO_4$ tetrahedra, tetrahedra themselves sharing one corner to form $M_2O_7$ units. However, several workers realized that the symmetry of these structures would lead to unrealistically short $M$–O–$M$ bridging bond lengths. The solution to this problem was first suggested by Vollenke (9) who reported that many of these systems have tripled supercells relative to the smaller cubic cell. The resulting reduction in symmetry allows certain $M_2O_7$ groups in the unit cell to bend their central $M$–O–$M$ bridge away from the ideal angle of 180°. Owing to the relative complexity of these tripled structures, few of these materials have had their full structures determined. Tillmans (10) solved the cubic structure of $SiP_2O_7$; Evans and co-workers solved the structure of $ZrV_2O_7$ by single-crystal methods (11); the structure of $TiP_2O_7$ has been investigated using $^{31}$P NMR and both powder and single-crystal methods (4, 6, 7). The assumption that all $A$(IV)$M_2O_7$ systems have a tripled cubic supercell at low temperature was recently questioned by the findings of Losilla and co-workers who reported that the pseudo-cubic $\gamma$-$GeP_2O_7$ (5) was in reality of lower symmetry. $^{31}$P NMR experiments have shown that the true room temperature symmetry of the pseudo-cubic $3\times3\times3$ superstructure of $ZrP_2O_7$ is *Pbca* (12). Both $ZrP_2O_7$ and $ZrV_2O_7$ have also been found to exhibit incommensurately modulated structures at intermediate temperatures (13, 14). The mixed valent $SbP_2O_7$ has also been reported as having a $1\times2\times1$ orthorhombic or monoclinic superstructure (15).

As part of a program to understand the factors controlling these fascinating structural subtleties, we have re-examined the $SnP_2O_7$ system (16) using X-ray, electron and neutron diffraction methods. These reveal that $SnP_2O_7$ undergoes a series of reversible phase transitions on heating and cooling, and has structures which differ from other members of the family.

## EXPERIMENTAL

A variety of synthetic procedures were investigated to achieve crystalline, high-purity samples of $SnP_2O_7$ suitable for detailed investigation. Samples prepared from $SnO_2$ and $(NH_4)_2HPO_4$ by heating in the temperature range from 873 to 1623 K were invariably found to contain small impurities of $SnO_2$. We presume this is due to phosphorus loss at high temperatures. Higher-purity samples could be prepared from tin tetrachloride and concentrated phosphoric acid. In a typical preparation, $SnCl_4\cdot5H_2O$ (98% +; Aldrich) and

[1] To whom correspondence should be addressed. Fax: (44) 191 384 4737. E-mail: john.evans@durham.ac.uk.



0022-4596/02 $35.00

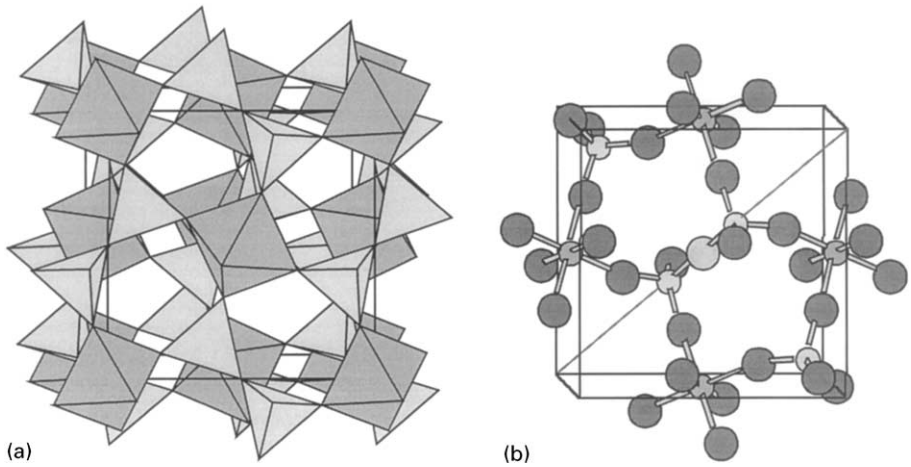


**FIG. 1.** The ideal high-temperature structure of $AM_2O_7$ phases can be described in terms of corner sharing $AO_6$ octahedra and $M_2O_7$ groups.

$H_3PO_4$ (85% w/w; Aldrich) were mixed with a Sn:P ratio of 1:3 and heated at 2 K/min to 598 K and held at this temperature overnight. The resultant fluffy white powder was reground and heated at temperatures in the range 598–1473 K for 60 h and then air quenched from the furnace. Single-phase samples of cubic $SnP_2O_7$ could be prepared over the entire temperature range; excess P is presumably lost during high-temperature firing. Samples investigated in detail in this study were sintered at 1473 K. Samples sintered at lower temperatures were found to show lower crystallinity and subtle differences in superstructure reflections.

## CHARACTERIZATION METHODS

Sample purity and crystallinity was confirmed using a Siemens d5000 diffractometer equipped with Cu$K\alpha$ radiation and a graphite diffracted beam monochromator. The room temperature cell parameter of $SnP_2O_7$ was determined from data collected from 10 to 120° $2\theta$ with a step size of 0.02° and a time per step of 10 s. Using a Si ($a = 5.43094$ Å) internal standard a cell parameter of 7.9444(1) Å was obtained.

Variable temperature X-ray diffraction studies were performed between 100 and 1050 K using a Bruker D8 advanced diffractometer equipped with an incident beam Ge(111) monochromator and a Braun linear position sensitive detector. Data were collected between 100 and 690 K using an Anton Paar TTK450 cryofurnace on samples sprinkled on an Al plate. Data between 300 and 1050 K were collected using an Anton Paar HTK1200 environmental furnace on samples sprinkled on amorphous $SiO_2$ disks. In a typical series of high-temperature experiments the material was warmed from 300 to 1050 K then cooled back to 300 K in 10 K intervals with $\sim$ 20 min data collections from 10 to 120° $2\theta$ (step = 0.0143°) at each temperature. A ramp rate of 0.05 K/s and equilibration time of 180 s at each temperature were used, giving a total experiment time of $\sim$ 80 h. Longer scans were performed before and after heating/cooling cycles to verify that no irreversible changes occurred during heating. Longer scans were also recorded at selected intermediate temperatures.

To obtain an accurate measurement of the true sample temperature (which can often differ significantly from that of even closely positioned thermocouples in non-ambient X-ray diffraction studies) an $Al_2O_3$ internal standard was employed. Data were corrected using the thermal expansion values provided by Taylor (17). Independent checks using a variety of well characterized materials suggest that temperatures quoted are accurate to 5 K. Good agreement was found between phase transition temperatures observed by X-ray and neutron diffraction measurements.

Since $SnP_2O_7$ shows at least three different subtle structural distortions as a function of temperature (*vide infra*), derivation of accurate thermal expansion data is somewhat complex. Variable temperature cell parameter values quoted in this paper were derived from X-ray data by Rietveld refinement of a model with atomic coordinates fixed at positions of the "ideal" cubic high temperature structure. Strong subcell reflections from 300 to 550 K on warming could be well fitted by a cubic unit cell; from 550 to 830 K by a triclinic cell; and above 830 K by a rhombohedral cell. Subtly different behavior was obtained on cooling. However, accurate cell volumes could be conveniently obtained over the whole temperature range using a triclinic cell with $a \sim b \sim c$; $\alpha \sim \beta \sim \gamma \sim 90°$. The "cell parameter" as a function of temperature is then quoted as $(V_{tric})^{1/3}$. These values were essentially identical to those obtained using different metric symmetries for different temperature ranges. The $Al_2O_3$ internal standard was included as a second crystallographic phase during refinement, and showed no discrepancies in cell parameters between warming and cooling.

Time-of-flight neutron diffraction data were collected on the high resolution powder diffractometer (HRPD) at the ISIS neutron facility, Rutherford Appleton Labs, UK. Approximately 11 g of sample was loaded into a standard vanadium sample can and placed into a Rutherford Furnace. Data were collected at room temperature for approximately 150 μA h ( ~ 4 h) using a time of flight range of 34,000–120,000 μs ($d = 0.70$–$2.49$ Å). Variable temperature diffraction data were recorded from 373 to 1243 K in 10 K steps. The sample was heated to the required temperature, allowed to equilibrate for 5 min, and data collected for 9 μA h ( ~ 15 min). When these measurements were complete the sample was cooled to 1003 K and data collected for 140 μA h. Diffraction data at this temperature were identical to those recorded on warming. Instrument constants were calibrated relative to a 7.9444 Å room temperature cell parameter. Cell parameters as a function of temperature were determined using the same strategy as employed for X-ray data.

Determination of the unit-cell parameters in the temperature regions where the sample subcell reflections showed splitting is complicated by the small deviations from cubic symmetry compared to the reflection full-width at half-maximum. At high temperature, the rhombohedral splitting pattern could be derived by inspection. For the intermediate temperature region, cells reported in this paper were determined by a simulated annealing procedure in which atomic coordinates were fixed at values for the ideal structure and a Rietveld refinement performed in space group $P1$. After convergence, cell edges were set to a random value between 7.95 and 8.01 Å and cell angles to random values between 89.5 and 90.5°, and the structure re-refined. This procedure was performed several thousand times. The cell with the lowest $R$-factor explained the observed peak splittings well. An identical protocol was performed with neutron data and essentially the same cell distortion found. In the high-temperature region this protocol did not reveal any triclinic cell significantly better than the rhombohedral cell obtained by inspection.

All crystallographic refinements were performed within the Topas software suite (18).

Thermal analysis of the samples was performed using a Mettler Toledo DSC25 differential scanning calorimeter (DSC) controlled by a Mettler Toledo TC15 TA controller. Data were collected in the temperature range 298–823 K using a heating and cooling rate of 5 K/min. Thermogravimetric analysis (TGA) was performed using a Perkin-Elmer Pyris 1 Thermogravimetric analyzer. The sample was placed in a platinum pan examined in the temperature range 303–1073 K both on heating and cooling. No significant weight loss was observed in this region.

Electron microscope samples were prepared by crushing and dispersing onto holey-carbon coated molybdenum grids which were subsequently examined using a Philips EM430 transmission electron microscope (TEM).

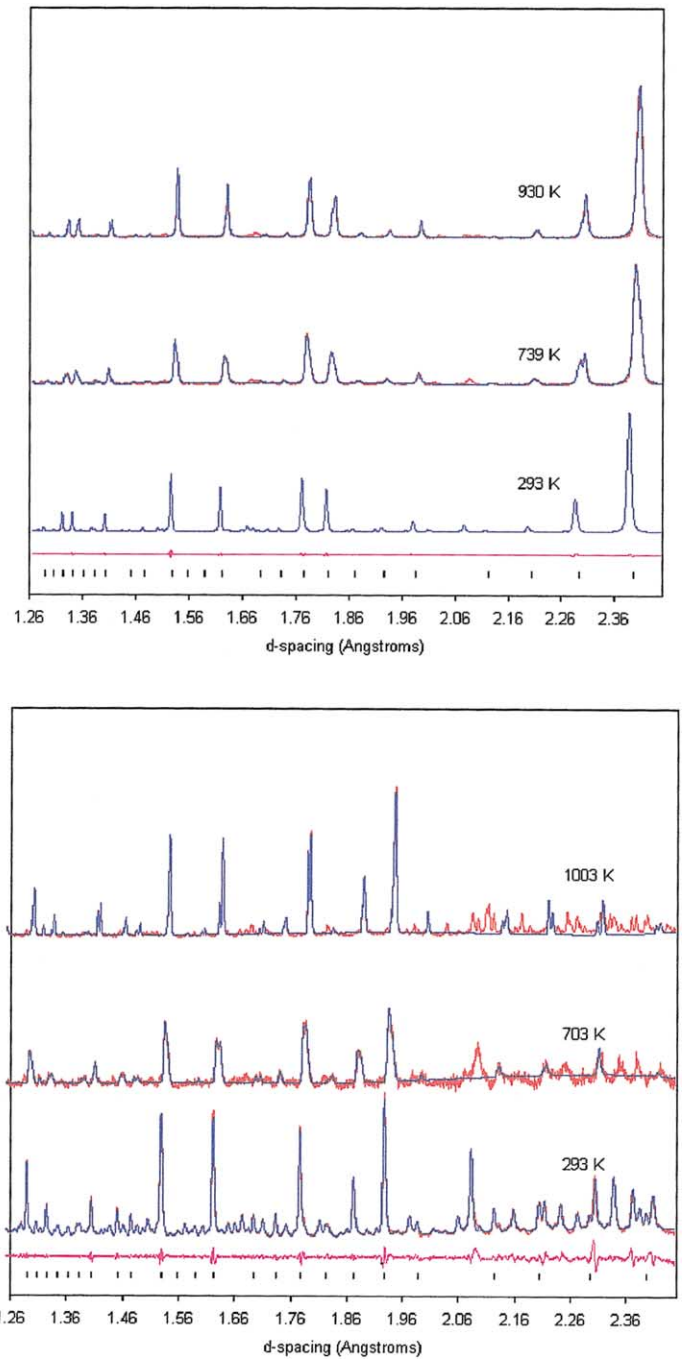


**FIG. 2.** Pawley fits to X-ray and neutron powder diffraction data collected at various temperatures. Tick marks show reflections predicted by the simple cubic cell at each temperature. X-ray and time of flight neutron data have been converted to $d$-spacing for ease of comparison. Data at 293 K fitted to $3 \times 3 \times 3$ superstructure, other temperatures to triclinic/rhombohedral subcells discussed in the text. Neutron data at 703 K were recorded for 15 min as compared to 4 h at 293 and 1003 K. Observed data shown as solid red line, calculated as blue and room temperature difference curve as pink. Significant discrepancies in room temperature neutron fits are seen around 2.3 Å.

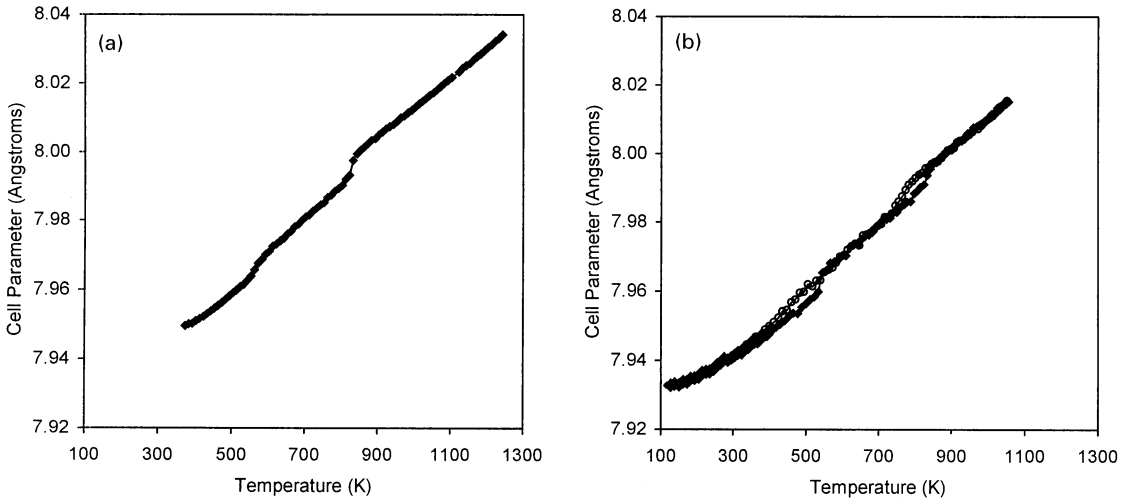


**FIG. 3.** (a) Unit-cell parameter as derived from neutron diffraction data as sample is warmed from 373 to 1243 K and (b) from X-ray data on both warming (filled points) and cooling (open points) the sample.

## RESULTS

Selected X-ray and neutron powder diffraction patterns of $SnP_2O_7$ are shown in Fig. 2, and the linear thermal expansion in Fig. 3. It is clear from these data that $SnP_2O_7$ undergoes two phase transitions between 100 and 1243 K. Differential scanning calorimetry showed no significant thermal events on either heating or cooling which suggests that these phase transitions are second order or higher. The linear thermal expansion from X-ray data (defined as $[(a_{T2} - a_{T1})/a_{T1}(T_2 - T_1)]$) between 305 and 1001 K is $1.25 \times 10^{-5}\,K^{-1}$.

At room temperature both X-ray and neutron diffraction data show a family of strong reflections that are associated with the simple cubic subcell, with a cell parameter at 298 K of $a = 7.9444$ Å. In addition to these reflections, a family of

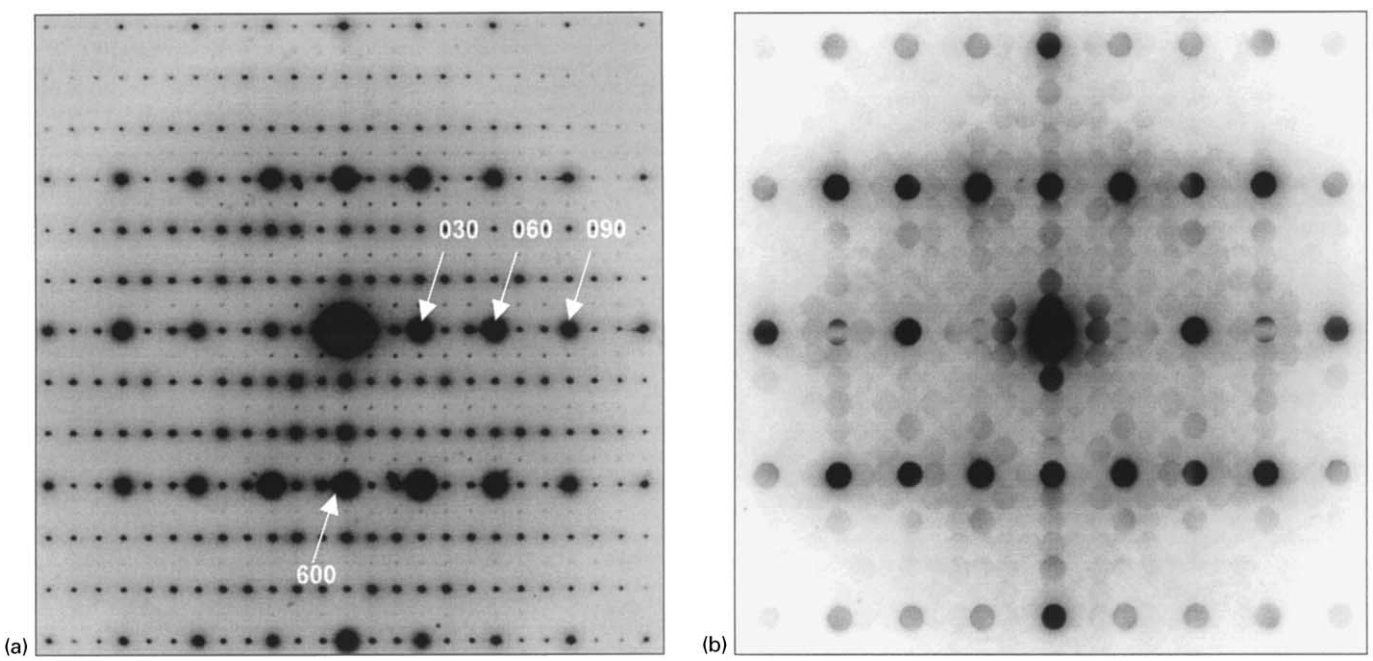


**FIG. 4.** Typical (a) ⟨001⟩ zone axis selected area electron diffraction pattern and (b) the corresponding ⟨001⟩ zone axis micro-diffraction pattern (⟨100⟩* or $a^*$ down the page, ⟨010⟩* or $b^*$ horizontal). Note that there is no extinction condition on the ⟨$hk0$⟩* reflections, requiring that the a-glide expected for space group $Pa\bar{3}$ is definitely not present. Gjonnes–Moodie lines running through the 030 and 090 disks of (b) are clearly visible.

weaker supercell reflections are clearly visible. Electron diffraction data show that the weak reflections are due to a $3 \times 3 \times 3$ superstructure, in common with several other members of the $AM_2O_7$ family. There are, however, distinct differences to those members of the family, which have been previously studied. Firstly $\langle 001 \rangle$ type zone axis electron diffraction patterns (EDPs) such as that shown in Fig. 4a clearly show that there is no extinction condition on the $\langle hk0 \rangle^*$ reflections, requiring that the *a*-glide expected for space group $Pa\bar{3}$ is definitely not present. Figure 4b shows a corresponding $\langle 001 \rangle$ zone axis microdiffraction pattern. Gjonnes–Moodie lines running through the center of the 030 and 090 disks confirm that the $2_1$ axis along $b^*$ remains intact. The absence of similar Gjonnes–Moodie lines along the $a^*$ direction of Fig. 4b initially made us think that the $2_1$ axis along $a^*$ might be broken. The absence of $h00$ $h =$ odd reflections in careful off-axis $\langle 100 \rangle^*$ systematic row electron diffraction patterns, however, indicates that the $2_1$ axis along *a* is also present. Electron diffraction studies thus suggest that the room temperature space group is $P2_13$ or possibly $P2_12_12_1$. Some weak evidence for this latter space group can be inferred from a careful measurement of EDPs such as that shown in Fig. 4a which suggests that $b^*$ may be slightly larger than $a^*$. However, it is difficult to place much reliance upon this. To date no other member of the $AM_2O_7$ family with a $3 \times 3 \times 3$ superstructure has been reported to have this, or a compatible lower symmetry space group. Figure 2 shows Pawley (19) fits to the room temperature X-ray and neutron diffraction data of $SnP_2O_7$. Whilst all superstructure peaks in the X-ray pattern can be well fitted by a $3 \times 3 \times 3$ cubic superstructure, there are small but significant discrepancies in regions of the neutron diffraction data suggesting that the true room temperature symmetry of $SnP_2O_7$ may be lower than cubic.

As can be seen from Figs. 2, 3, 5 and 6, a marked change in both X-ray and neutron patterns occurs at approximately 550 K. Several of the subcell reflections (e.g. those at 1.78, 1.87 and 1.93 Å of Fig. 2b) are seen to broaden/split and several supercell reflections also undergo a marked change, indicating the onset of a structural phase transition. Examination of the splitting patterns of neutron and X-ray data

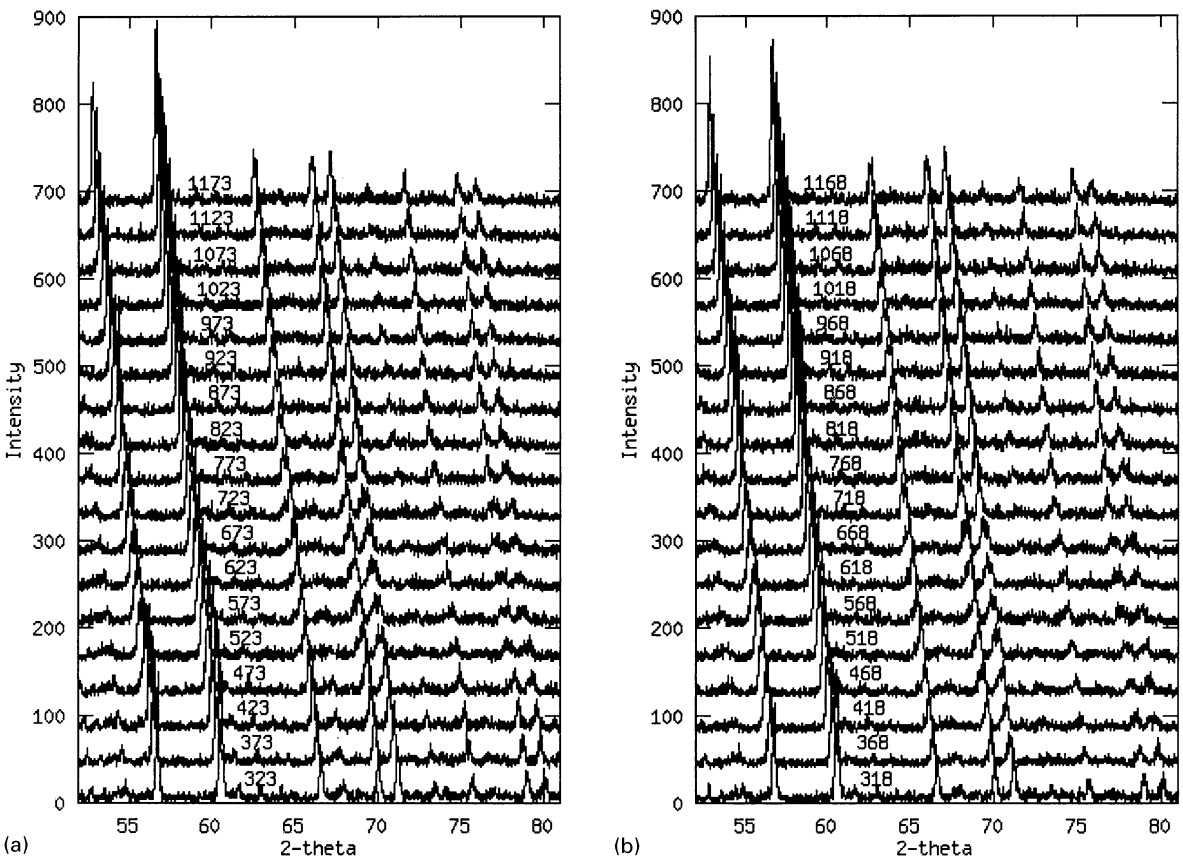


**FIG. 5.** X-ray diffraction data recorded at 10 K intervals from (a) 323 to 1173 K on warming and (b) 1168 to 318 K on cooling. Every fifth data set is shown; data have been offset by $-0.2^\circ/50$ K in $2\theta$ for clarity. The onset of the triclinic region on warming can be seen by the broadening of reflections in the 523 K data set (e.g. those at $\sim 77^\circ$ $2\theta$); the rhombohedral peak splitting is clearly visible at 873 K, at which temperature the $\sim 77^\circ$ $2\theta$ peaks have sharpened. On cooling the material appears to retain a rhombohedral splitting at 768 K and shows a more gradual reversion to cubic symmetry.

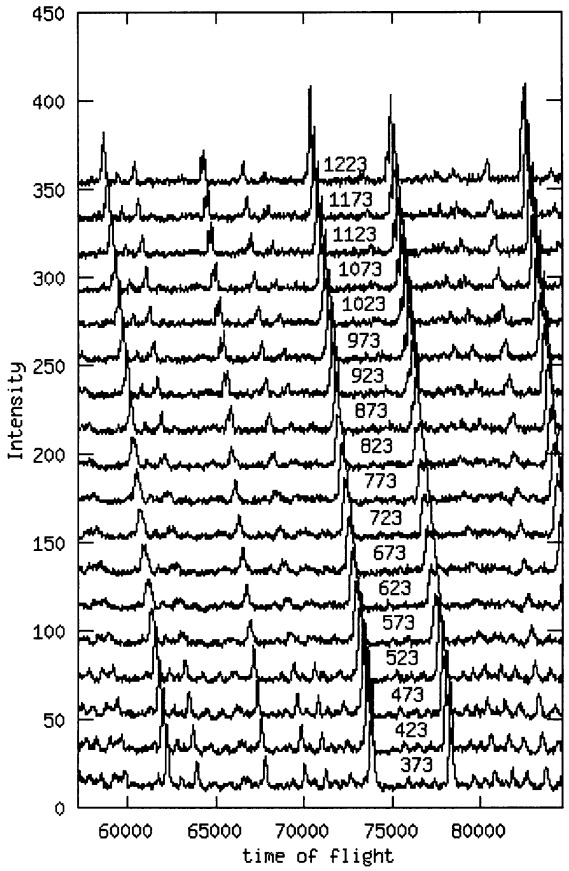


**FIG. 6.** Neutron diffraction data recorded between 373 and 1223 K on warming. Time-of-flight range corresponds to a *d*-spacing of 1.76 to 1.19 Å, an identical *d*-spacing range to data of Fig. 5. Data have been offset by − 250 μs/50 K for clarity.

suggests that the subcell reflections can be explained in terms of a triclinic cell with $a = 7.9804$ Å, $b = 7.9708$ Å, $c = 8.003$ Å, $\alpha = 90.08°$, $\beta = 90.38°$, $\gamma = 90.10°$ (values quoted at 739 K from X-ray data). Pawley fits to this cell are included in Fig. 2. In the absence of a full structural determination (which is beyond the possibilities of the current data), this is the best cell obtainable. There will, however, be some correlation between cell parameters and atomic coordinates used during the simulated annealing used in its determination. This cell does give good agreement with data from 550 to 830 K. We note that the related monoclinic cell (with $\alpha = \gamma = 90°$), whilst giving a reasonable fit to X-ray/neutron data fails, for example, to explain the splitting of the 222 reflection at $\sim 39°$ $2\theta$ in the X-ray data, the full-width at half-maximum of which suggests more than the two reflections expected for monoclinic symmetry.

On warming to 830 K a second structural change is apparent from powder diffraction data. Above this temperature the subcell reflections can be described using a rhombohedral cell with $a = 8.0132$ Å, $\alpha = 90.18°$ (values quoted at 1073 K). Supercell reflections are also visible at this temperature. Subcell reflections retain this rhombohedral splitting pattern to the highest temperatures recorded.

On cooling, significant hysteresis is observed in the pseudo-cubic cell parameters. Preliminary experiments suggest that this is largely independent of cooling rate. These effects are readily visible in the powder XRD spectra recorded on warming and cooling the material shown in Fig. 5. Whilst the cell volume per formula unit in the intermediate temperature regime structure on warming and cooling is essentially identical, careful analysis of the powder diffraction data shows that the nature of the splitting of subcell reflections differs (Figs. 5 and 3b). In addition, the phase transition back to the room temperature $3 \times 3 \times 3$ superstructure on cooling is less abrupt. This effect can be clearly seen from a plot of subcell reflection full-width at half-maximum using a simple cubic model as a function of temperature as shown in Fig. 7. We note that whilst considerable hysteresis is observed in cell parameters and peak splitting patterns on heating and cooling, the room temperature cell parameter before and after a heating cycle is identical to within experimental error. The position and intensities of room-temperature superstructure reflections were also found to be identical at the beginning and end of each experiment, suggesting no irreversible change in the sample on heating. Identical cell parameter changes were observed under a dynamic vacuum of $10^{-2}$ mbar to those obtained in air. In addition, no discrepancies were observed in the cell parameters of the internal standard between heating and cooling cycles.

## DISCUSSION AND CONCLUSIONS

$SnP_2O_7$ again demonstrates the structural complexity of the $AM_2O_7$ family of materials. It seems logical to assume

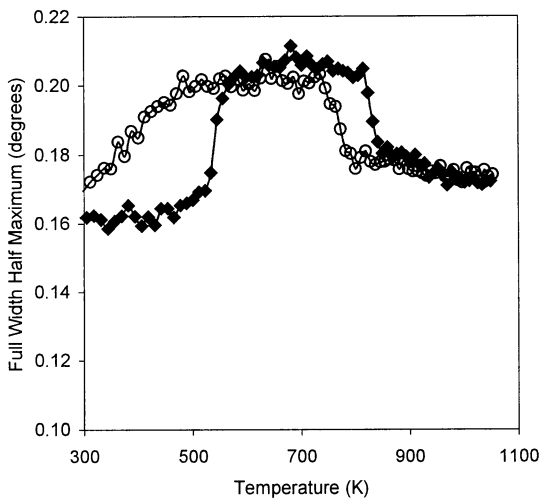


**FIG. 7.** Full-width at half-maximum of X-ray diffraction peaks as a function of temperature on both warming (closed points) and cooling (open points).

that at sufficiently high temperature the material would adopt a simple $\sim 8$ Å cubic unit cell, as has been described for members of the series such as $ZrP_2O_7$ and $ZrV_2O_7$. Under ambient pressure conditions, however, the material decomposes before this temperature limit can be reached. The structural phase transitions on cooling are, however, different to other members of the family studied to date. The principal driving force for these phase transitions can be considered to be the bending of P–O–P bonds of $P_2O_7$ groups which are required by symmetry to be 180° in the high-temperature structure. As these linkages bend, $AO_6$ and $PO_4$ polyhedra can undergo a coupled "folding" motion with only minimal internal distortion, which rapidly lowers the volume of the material. The observation that the lowest frequency quasi-rigid unit modes (QRUMs) (20, 21) of the parent phase have a modulation wave vector in the region of $\langle \frac{1}{3}, \frac{1}{3}, 0 \rangle^*$ suggests that forces opposing polyhedral motion are lowest in this region of reciprocal space, and has been used to rationalize the adoption of the low-temperature $3 \times 3 \times 3$ superstructure for many of these phases (14). Many of the systems studied to date (e.g. $SiP_2O_7$, $TiP_2O_7$, $ZrV_2O_7$) have been shown to adopt the simplest $3 \times 3 \times 3$ cubic superstructure (space group $Pa\bar{3}$) in which the point group of the high-temperature phase is retained, but 26/27ths of the translational symmetry elements and 2/3rds of the three-fold axes are destroyed. Others (e.g. $ZrP_2O_7$, $GeP_2O_7$) have been shown to exhibit lower symmetry $3 \times 3 \times 3$ superstructures (5, 12). In addition, $ZrP_2O_7$ and $ZrV_2O_7$ have both been shown to exhibit complex incommensurately modulated structures at certain temperatures (13,14). At the current time we cannot eliminate incommensurate modulations as being the origin of the discrepancy between peak splittings in the intermediate temperature regime ($550 < T < 830$ K) on warming and cooling.

The driving force for adopting these lower symmetry structures, and presumably the driving force for the complex series of triclinic/rhombohedral subcell reflection splittings in $SnP_2O_7$, are perhaps related to distortion energies of the $AO_6/MO_4$ polyhedra themselves. Distance least-squares (DLS) calculations show that even in a cubic $3 \times 3 \times 3$ superlattice, some distortion of $AO_6$ and $MO_4$ tetrahedra is required. The overall structural energy of $AM_2O_7$ superstructures will therefore be determined by four separate factors: the energy penalty involved in bending $M$–O–$M$ linkages, the bending potential of $A$–O–$M$ linkages and the energy penalties associated with distorting $AO_6$ and $MO_4$ tetrahedra (22). As these materials increase in volume due to the "unfolding" of their polyhedral linkages on warming, the balance of these contributions must change, leading to the unusual series of structural phase transitions observed for $SnP_2O_7$.

## ACKNOWLEDGMENTS

We acknowledge the EPSRC for funding and for access to neutron beam time and Kevin Knight for assistance with data collections.

## REFERENCES

1. V. Korthuis, N. Khosrovani, A. W. Sleight, N. Roberts, R. Dupree, and W. W. Warren, *Chem. Mater.* **7,** 412–417 (1995).
2. A. W. Sleight, *Curr. Opin. Solid State Mater. Sci.* **3,** 128–131 (1998).
3. J. S. O. Evans, *J. Chem. Soc. Dalton Trans.* 3317–3326 (1999).
4. S. T. Norberg, G. Svensson, and J. Albertsson, *Acta Crystallogr. Sect. C-Cryst. Struct. Commun.* **57,** 225–227 (2001).
5. E. R. Losilla, A. Cabeza, S. Bruque, M. A. G. Aranda, J. Sanz, J. E. Iglesias, and J. A. Alonso, *J. Solid State Chem.* **156,** 213–219 (2001).
6. J. Sanz, J. E. Iglesias, J. Soria, E. R. Losilla, M. A. G. Aranda, and S. Bruque, *Chem. Mater.* **9,** 996–1003 (1997).
7. X. Helluy, C. Marichal, and A. Sebald, *J. Phys. Chem. B* **104,** 2836–2845 (2000).
8. G. R. Levi and G. Peyronel, *Z. Krist.* **92,** 190–209 (1935).
9. H. Vollenke, A. Wittmann, and H. Novotny, *Monatsh. Chem.* **94,** 956–963 (1963).
10. E. Tillmanns, W. Gebert, and W. H. Baur, *J. Solid State Chem.* **7,** 69–84 (1974).
11. J. S. O. Evans, J. C. Hanson, and A. W. Sleight, *Acta. Crystallogr. B* **54,** 705–713 (1998).
12. I. J. King, F. Fayon, D. Massiot, R. K. Harris, and J. S. O. Evans, *Chem. Commun.* 1766–7 (2001).
13. R. L. Withers, J. S. O. Evans, J. Hanson, and A. W. Sleight, *J. Solid State Chem.* **137,** 161–167 (1998).
14. R. L. Withers, Y. Tabira, J. S. O. Evans, I. J. King, and A. W. Sleight, *J. Solid State Chem.* **157,** 186–192 (2001).
15. A. Verbaere, S. Oyetola, D. Guyomard, and Y. Piffard, *J. Solid State Chem.* **75,** 217–224 (1988).
16. C. H. Huang, O. Knop, D. A. Othen, F. W. D. Woodhams, and R. A. Howie, *Can. J. Chem.* **53,** 79–91 (1975).
17. D. Taylor, *Br. Ceram. Trans. J.* **83,** 92–98 (1984).
18. Bruker AXS Ltd., "Topas V2.0: General Profile and Structure Analysis Software for Powder Diffraction Data" Bruker AXS, Karlsruhe, 2000.
19. G. S. Pawley, *J. Appl. Crystallogr.* **14,** 357–361 (1981).
20. M. T. Dove, V. Heine, and K. D. Hammonds, *Miner Mag.* **59,** 629–639 (1995).
21. K. D. Hammonds, M. T. Dove, A. P. Giddy, V. Heine, and B. Winkler, *Am. Mineral.* **81,** 1057–1079 (1996).
22. D. K. Seo and M. H. Whangbo, *J. Solid State Chem.* **129,** 160–163 (1997).